Phenotyping and modeling of root hydraulic architecture reveal critical determinants of axial water transport

Yann Boursiac, Christophe Pradal, Fabrice Bauget, Mikaël Lucas, Stathis Delivorias, Christophe Godin, Christophe Maurel

HAL Id: hal-03701955
https://hal.inrae.fr/hal-03701955

Submitted on 22 Jun 2022

Plant Physiology®

Research Article

Phenotyping and modeling of root hydraulic architecture reveal critical determinants of axial water transport

Yann Boursiac [iD] ,[1,§] Christophe Pradal [iD] ,[2,3,4,§] Fabrice Bauget,[1,#] Mikaël Lucas [iD] ,[1,†,#]
Stathis Delivorias [iD] ,[1] Christophe Godin [iD] [3,‡] and Christophe Maurel [iD] [1,*]

1   Institute for Plant Sciences of Montpellier (IPSiM), Univ Montpellier, CNRS, INRAE, Institut Agro, Montpellier 34060, France
2   CIRAD, UMR AGAP Institut, Montpellier 34398, France
3   Inria Project-team Virtual Plants, UMR AGAP, Univ Montpellier, INRIA, CIRAD, INRAE, Montpellier 34398, France
4   Inria and LIRMM, Univ Montpellier, CNRS, Montpellier 34095, France

*Author for correspondence: christophe.maurel@cnrs.fr
†Present address: UMR DIADE, Univ Montpellier, IRD, Montpellier, France.
‡Present address: Laboratoire Reproduction et Développement des Plantes, Univ Lyon, ENS de Lyon, UCB Lyon 1, CNRS, INRAE, Inria, Lyon, France.
§Y.B, and C.P contributed equally as first authors.
#F.B., and M.L. contributed equally but not as first authors.
Y.B. contributed to model coding, developed the cut-and-flow and root intercept approaches, and contributed to phenotyping characterizations. C.P. supervised the coding of the HydroRoot model and contributed to data analyses. F.B. finalized model coding, performed sensitivity analyses, and contributed to cut-and-flow analyses. M.L. developed the first HydroRoot model version and performed root anatomy analyses. S.D. performed the analysis of root intercept numbers. C.M. and C.G. designed the study which was regularly discussed with Y.B. and C.P. C.M. wrote the article with contributions of all the authors.
The author responsible for distribution of materials integral to the findings presented in this article in accordance with the policy described in the Instructions for Authors (https://academic.oup.com/plphys/pages/General-Instructions) is: Christophe Maurel (christophe.maurel@cnrs.fr).

Abstract

Water uptake by roots is a key adaptation of plants to aerial life. Water uptake depends on root system architecture (RSA) and tissue hydraulic properties that, together, shape the root hydraulic architecture. This work investigates how the interplay between conductivities along radial (e.g. aquaporins) and axial (e.g. xylem vessels) pathways determines the water transport properties of highly branched RSAs as found in adult Arabidopsis (*Arabidopsis thaliana*) plants. A hydraulic model named HydroRoot was developed, based on multi-scale tree graph representations of RSAs. Root water flow was measured by the pressure chamber technique after successive cuts of a same root system from the tip toward the base. HydroRoot model inversion in corresponding RSAs allowed us to concomitantly determine radial and axial conductivities, providing evidence that the latter is often overestimated by classical evaluation based on the Hagen–Poiseuille law. Organizing principles of Arabidopsis primary and lateral root growth and branching were determined and used to apply the HydroRoot model to an extended set of simulated RSAs. Sensitivity analyses revealed that water transport can be co-limited by radial and axial conductances throughout the whole RSA. The number of roots that can be sectioned (intercepted) at a given distance from the base was defined as an accessible and informative indicator of RSA. The overall set of experimental and theoretical procedures was applied to plants mutated in *ESKIMO1* and previously shown to have xylem collapse. This approach will be instrumental to dissect the root water transport phenotype of plants with intricate alterations in root growth or transport functions.

Open Access

Introduction

Water uptake by roots represents a key adaptation of plants to aerial life. Taking place at the plant–soil interface, this process is highly dependent on the root system architecture (RSA). Most root systems are highly complex, branched structures with, for instance, thousands of ramifications and a cumulated length of several hundreds of meters for a single maize (*Zea mays*) plant. These systems are also highly dynamic. In particular, water availability interferes with the orientation and rate of primary root growth and the frequency and symmetry of root branching thereby promoting water resource foraging (Klein et al., 2020; Maurel and Nacry, 2020). The ability of root systems to reach deep soil layers at reduced cost was proposed to be a key trait for acclimation to water-deprived environments (Lynch, 2013). Yet, a comprehensive view of how elementary water transport processes occur in root tissues and integrate within the RSA, thereby shaping the root hydraulic architecture, is needed to fully comprehend the water uptake capacity of plants.

Water uptake and its subsequent transport within the plant are determined by the gradient of water potentials throughout the soil–plant–atmosphere-continuum (Steudle, 2001; Draye et al., 2010). Following radial transport across peripheral cell layers (epidermis, cortex, and endodermis), soil water reaches the stele and xylem vessels where it is transported axially to the plant aerial parts. These radial and axial processes, that are often presented sequentially, actually operate simultaneously and throughout the whole RSA. In most physiological studies of root water transport, axial conductance was inferred from xylem vessel size using the Hagen–Poiseuille law (Steudle and Peterson, 1998; Lefebvre et al., 2011; Klein et al., 2020). Because it is the site for formation of xylem vessels, the root tip was identified as the main resistive place for axial water transport whereas axial limitation was supposedly negligible in older root segments due to the presence of large metaxylem vessels (Steudle and Peterson, 1998). In contrast, radial transport which is often represented as a combination of cell-to-cell and cell wall (apoplastic) paths running in parallel, was proposed to explain fundamental hydraulic properties of the whole root (Steudle and Peterson, 1998; Barrowclough et al., 2000; Knipfer and Fricke, 2011).

Several types of numerical hydraulic models have been developed to address the complexity of root water uptake, and radial transport in particular. Whereas early models integrated concentric hydraulic resistances within a root radial section (Steudle and Jeschke, 1983; Jones et al., 1988; Bramley et al., 2009), modeling was recently applied to a more precise, cell-based view of the root radial anatomy (Couvreur et al., 2018; Heymans et al., 2021). Biophysical models have also addressed water transport at whole root level. With respect to models that describe the functioning of root segments (Frensch and Steudle, 1989; Zwieniecki et al., 2003; Zarebanadkouki et al., 2014) or use a simplified representation of root system hydraulics (Knipfer and Fricke, 2011), Doussan et al. integrated an explicit description of RSA with hydraulics. To be linked to soil water transfer, hydraulic functioning of the root had, however, to be reduced to simplified radial and axial processes (Doussan et al., 1998a, 1998b). Since then, there have been several attempts to refine the hydraulic functioning of elementary root segments at the whole root level (Zwieniecki et al., 2003; Draye et al., 2010; Javaux et al., 2013; Foster and Miklavcic, 2016; Bouda et al., 2018). More recently, Meunier et al. (2017b, 2017c) developed a hybrid analytical–numerical model of root water uptake with increased computational efficiency.

Despite these efforts, the respective limitations of axial and radial conductances and their precise contribution to whole root hydraulics remain key and as yet unresolved issues. Based on a porous pipe representation of unitary roots, Zwieniecki et al. (2003) showed that axial hydraulic limitation can lead to saturation of root conductance meaning that long roots do not provide any additional advantage in terms of overall flux intensity (Zwieniecki et al., 2003; Meunier et al., 2017a, 2018). This view was recently extended to entire root networks which, however, remained theoretical in nature (Bouda et al., 2018). While these modeling approaches point to key hydraulic properties of root systems, most of them were assessed with scarce or heterogeneous experimental data.

With respect to native, soil-imbedded root systems, roots excised from hydroponically grown plants are more easily amenable to accurate hydraulic measurements. In Arabidopsis (*Arabidopsis thaliana*) in particular, the pressure chamber technique has proved efficient for addressing fundamental root hydraulics properties in various genotypes or environmental conditions (Postaire et al., 2010; Sutka et al., 2011; Di Pietro et al., 2013). More specifically, this technique provides access to the whole root system hydraulic conductivity (Lp_r) and allows to take into account the contribution of fragile lateral roots.

Here, we used pressure chamber measurements coupled with a modeling approach to investigate how the interplay between radial and axial conductivities determines the water transport properties of complex and realistic RSAs. By combining experimental and computational modeling procedures, this work shows how radial and axial conductivities can be concomitantly determined and reveals contexts in which axial conductance can be limiting. The overall approach can also help dissect the root water transport phenotype of plants with complex alterations in root growth or transport functions.

Results

Mapping hydraulic properties on realistic models of RSAs

We first explored a set of 10 3-week-old, hydroponically grown Columbia-0 (Col-0) plants for which root water transport capacity was measured by the pressure chamber technique and RSA was captured by image analysis

(Figure 1A). The root systems of these plants exhibit a substantial complexity with total length up to 2.1 m, and up to 354 root extremities corresponding to a primary root carrying two orders of lateral roots (Table 1). We described quantitatively the individual RSAs by constructing dynamical multi-scale tree graphs (MTGs) (Godin and Caraglio, 1998). The graph nodes represented plant segments of 100 μm (equivalent to the range of a cell length) and contained information on the position of the different branching points (Godin et al., 1999; Danjon and Reubens, 2008; Lobet et al., 2015; Figure 1B). Microscopic observations indicated that diameters of the primary and lateral roots were fairly homogeneous within each branching order but were reduced by 30%–40% between successive orders, varying from 188 ± 22 μm ($\pm$SD; $n = 64$) in the primary root to as low as 69 μm in second order lateral roots. Thus, external root surfaces were calculated in the MTGs, assuming that root diameter was constant for a given root order, with a 30% decrease between successive root orders.
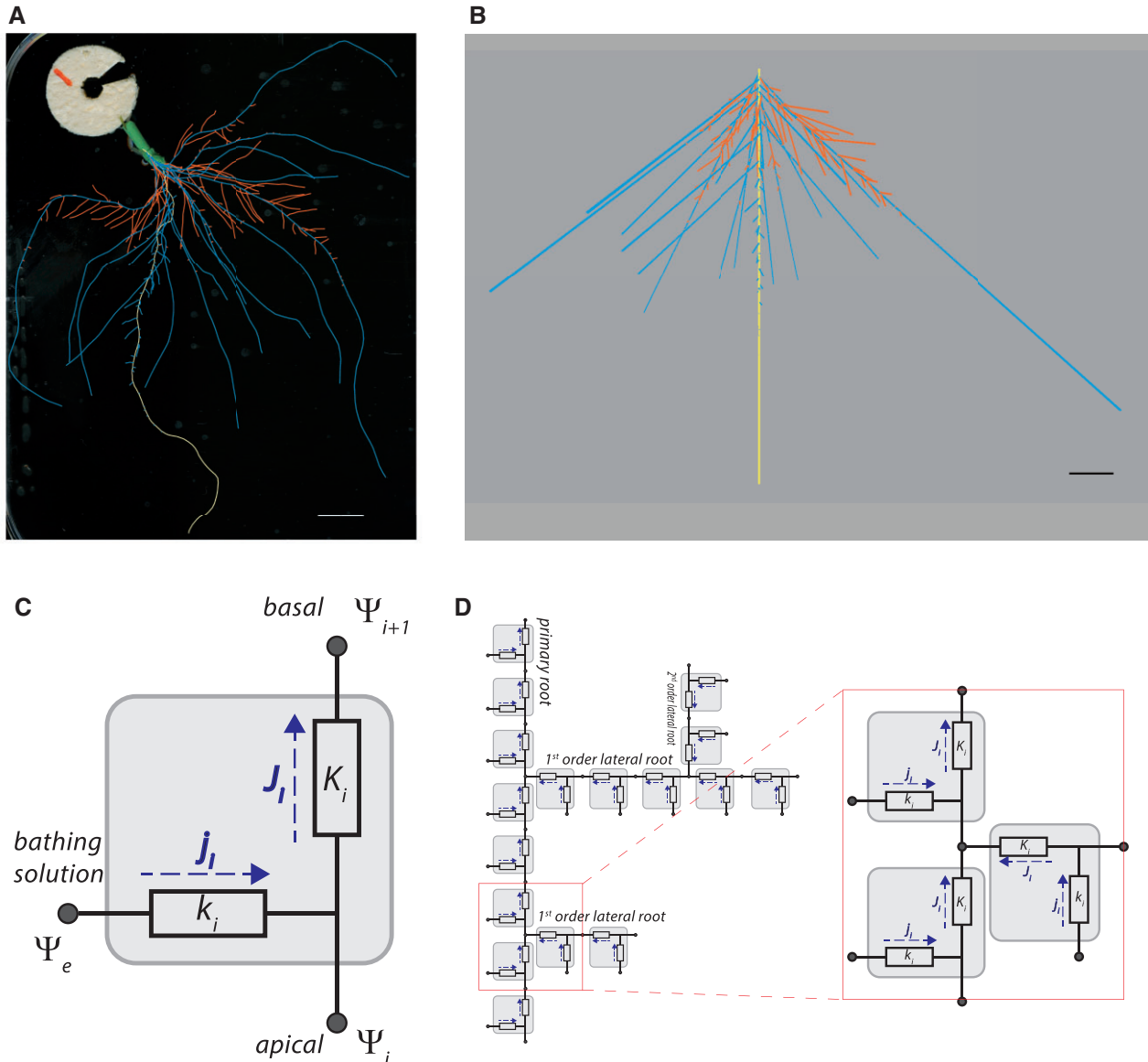
Figure 1 Modeling water transport in real RSAs. A, Representative RSA of a 21-day-old Arabidopsis plant grown in hydroponics. The excised root system was spread out in a petri dish and scanned. For clarity, the primary root, the first order, and second-order lateral roots are shown in yellow, light blue, and red, respectively. Scale bar: 10 mm. B, Bi-dimensional representation of the same digitized RSA. Note that the emergence angle of root segments is arbitrarily set. Same color conventions as in (A). Scale bar: 10 mm. C, Schematic representation of an elementary root segment of rank i consisting of a derivative microcircuit containing both radial (k_i) and axial (K_i) hydraulic conductances. Each segment is connected with the root bathing solution (exterior, at Ψ_e water potential) and basal and apical neighboring segments (at Ψ_i and Ψ_{i+1} water potentials, respectively, except for the last segments). Combination of k_i and $\Psi_e - \Psi_i$, or K_i and $\Psi_i - \Psi_{i+1}$ yield segment water uptake (j_i) and overall flow through the segment (J_i), respectively. D, Elementary root segments are inserted into a dynamical MTG builder of RSA to yield the HydroRoot model. The inset shows the specific case of a root ramification.

Table 1 Measured architectural parameters and calculated elementary hydraulic radial conductance (k) of individual root systems

Plant number	Total length (m)	Surface area (10^{-4} m^2)	Calculated k (10^{-8} m s^{-1} MPa^{-1})
#1	1.63	4.63	3.39
#2	1.88	5.18	7.08
#3	1.60	4.48	8.70
#4	0.71	2.20	5.59
#5	1.88	5.10	13.12
#6	1.12	3.36	8.30
#7	2.13	6.03	19.22
#8	2.11	6.05	22.13
#9	0.76	2.49	12.76
#10	0.78	2.59	4.03

Water flow was measured using the pressure chamber technique in excised root systems from the indicated individual plants (two biological replicates). RSAs were then exhaustively analyzed. The table summarizes integrated parameters from these measurements and the k values calculated using HydroRoot to match the measured water flows. The axial conductance was calibrated according to Hagen–Poiseuille law, and the same lowess fit profile, as shown in Supplemental Figure S1, was used for all RSAs.

Based on these detailed RSA representations, we developed a hydraulic model to simulate water fluxes in the corresponding segment network. In this model, called HydroRoot (https://github.com/openalea/hydroroot), each elementary root segment is associated with a derivative microcircuit containing both radial (k) and axial (K) hydraulic conductances. While the former (k) accounts for all pathways mediating radial water flow, the latter (K) represents the conductances of the segment xylem vessels (Figure 1C). Accordingly, each elementary root segment is connected with the root bathing solution, and with basal and apical neighboring segments (Figure 1C). Overall, an individual root is represented as a series of elementary units while root branching is considered as a derivation in the global circuit (Figure 1D). Moreover, root tips are considered as terminal segments, with an elementary radial flow that feeds into the axial flow of the neighboring segment. In addition, endogenous osmotic driving forces were not taken into account since spontaneous exudation was close to 0 in our conditions (Boursiac et al., 2005). Thus, the boundary variables of the hydraulic model are either imposed experimentally [homogeneous water potential (hydrostatic pressure) in the bathing solution; root base at equilibrium with atmospheric pressure] or are measured (outgoing water flow: $J_v(P)$). Based on these principles, HydroRoot can be run through a two-pass algorithm throughout the RSA, as previously described on aerial branching structures (Prusinkiewicz et al., 2007): equivalent conductances of the different branches are first computed in a backward pass (from root tips to base), followed by a forward pass (from root base to tips) computing the water potentials at each point of the root system. Due to the lack of capacitive components, water fluxes entering each elementary unit through radial or axial transport are equilibrated by the out-going axial flux toward the root base. The set of model parameters is recapitulated in Supplemental Table S1.

Parameterization of axial conductance (K) for deduction of root radial conductivity (k)

To parameterize axial conductances, xylem vessel number and size were sampled along the axis of primary, first and second-order lateral roots of five independently grown Col-0 plants. Supplemental Figure S1A shows typical xylem differentiation patterns from root tip to base. Xylem conductance was computed according to Hagen–Poiseuille law applied to the general case of elliptic conduits and implemented according to vessel number and size in each elementary unit, thereby providing a conductance profile along the root axis (Supplemental Figure S1B). Because it is linked to the fourth power of vessel radius, K shows a dramatic increase (>600-fold) from root tip to base. We found no clear distinction between K profiles, in terms of shape and magnitude, among different root orders and plants. Thus, a unique K profile derived from experimental data by locally weighted scatterplot smoothing (lowess) was applied along all root axes (Supplemental Figure S1B).

The direct determination of k is, at present, experimentally not achievable in species with highly branched and tiny roots such as Arabidopsis, as it would require to measure radial flows in root segments between consecutive branching points (~ 2 mm in the present case) (Meunier et al., 2018). We therefore estimated radial conductance values by inverse modeling, using the RSA and outgoing water flow [$J_v(P)$] data determined in the 10 plants described above. Considering that k is constant from the root base to tips, its value was determined in individual plants, as presented in Table 1, and ranged from 3.4 to 22.1 10^{-8} m s^{-1} MPa^{-1}, with an average of 10.4 ± 2.0 10^{-8} m s^{-1} MPa^{-1} ($\pm$SE).

Concomitant determination of axial and radial conductances by model inversion

Although based on well-established physical principles, the calculation of K presented above overlooks the finite length of xylem vessels and neglects possible hydraulic limitations occurring during water passage between adjacent vessels or at root branching sites (Shane et al., 2000). Previous authors have also found discrepancies between calculated and measured axial conductance (Frensch and Steudle, 1989; Tixier et al., 2013; Bouda et al., 2018). Here, we refined our approach to simultaneously determine axial and radial conductances by model inversion in individual and real RSAs. For this, we characterized root systems that were sequentially sectioned at a given distance from their bases. The overall procedure is illustrated in Supplemental Figure S2A. Figure 2, A and B, illustrates a series of pressure chamber measurements obtained after successive cuts of a same root system from the tip toward the base. The successive cuts create direct hydraulic connections between the cell bath and xylem lumen, and thereby $J_v(P)$ increases although overall root surface area progressively decreases (Supplemental Figure S2C and Figure 2, A and B). For reference, control intact roots systems that underwent the same successive
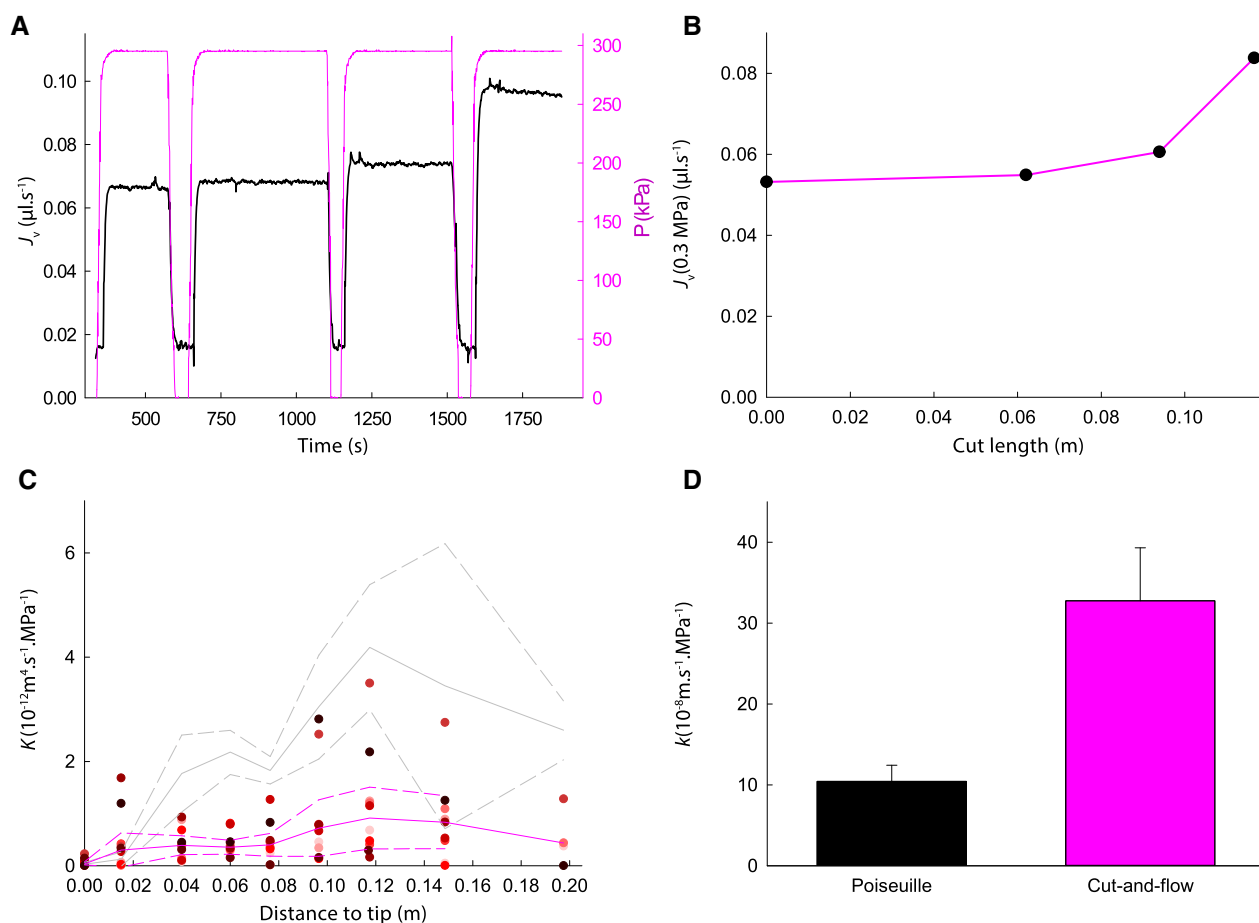
Figure 2 Determination of axial and radial conductances using cut-and-flow experiments. A, Kinetic measurement of pressure-induced sap flow (J_v) during a representative cut-and-flow experiment. J_v (black trace) was measured at constant pressure (magenta trace; $P = 0.3$ MPa). The intermittent drops in pressure (P) correspond to the maneuvers for opening the chamber and partial ablation of the root system. B, Corresponding plot of J_v as a function of the root length that was cut from the primary root tip. C, Profile of axial conductance (K) along the root axis as determined after parameter adjustment in cut-and-flow experiments. Data from 10 individual Col-0 plants, each being identified by a specific color. The figure shows (in magenta) the median K curve (solid line) and the 95% confidence interval (dashed lines). For reference, the lowess K profile and corresponding 95% confidence interval, as determined using Hagen–Poiseuille law (see Supplemental Figure S1B), are drawn in gray solid and dotted lines, respectively. D, Mean values of radial conductance ($k \pm$ se, $n = 10$) as determined by model inversion, using Hagen–Poiseuille law or cut-and-flow experiments for evaluation of K. The two values are statistically different (Student t test; $P < 0.01$).

pressurization cycles showed a constant $J_v(P)$ (Supplemental Figure S2B). Unlike previous analyses performed on elementary root segments (Frensch and Steudle, 1989; Meunier et al., 2018), the present experimental procedure results in a complex mix of sections of various root orders, made at the same distance from the root base, but at varying distances from their respective tip (Supplemental Figure S2). Thus, we used a parameter adjustment procedure on HydroRoot running with digitized architectures, either intact or with the indicated sections, to infer k (set constant over the overall RSA) and K (as a piecewise linear function of the distance to tip, see "Materials and methods"). The robustness of the multi-parameter adjustment procedure for K, almost independent of the first guess parameter values, is displayed in Supplemental Figure S3. When applied to 10 individual RSAs, this so-called cut-and-flow approach confirmed the variability in K profile previously observed between plants (Figure 2C). Most importantly, it pointed to adjusted

K values that were markedly lower than those calculated using Hagen–Poiseuille law, by a factor of 4–6. In relation to these new K estimates, k values inferred from the cut-and-flow approach were higher (mean value $\pm$ SE: 32.8 ± 6.5 10^{-8} m s^{-1} MPa^{-1}) than when using the first inversion method described above (Figure 2D).

Since a constant radial conductivity (k) represents a strong assumption of our model, we also investigated roots in which k was set constant in root tips but, due to suberization, dropped to a three times lower plateau value in the differentiated zone (Doussan et al., 1998b; Ranathunge and Schreiber, 2011; Heymans et al., 2021). Using such k profile and cut-and-flow data from the same 10 plants as above, we obtained a slightly but nonsignificantly reduced average plateau value of k (Supplemental Figure S4A). Moreover, this nonuniform k profile did not significantly modify the variation of K along the root axis (Supplemental Figure S4B). We interpret this to mean that the increase in $J_v(P)$

observed upon successive cuts of the RSA, and opening of vessels, is much more powerful to capture spatial variations of axial conductance (K) than k.

A general model of Arabidopsis RSA

In order to explore the combined impacts of k, K, and RSA on root water transport, we went on to apply the HydroRoot model to an extended, yet realistic, set of simulated RSAs. Our first step was therefore to develop a general model of Arabidopsis RSA.

To do this, we first explored the organizing principles of Col-0 RSA by observing primary and first and second order lateral roots in a set of 13 individual plants. When looking at the distribution of root branching, we observed that this process was always initiated between 8 and 40 mm from the root tip, and then developed at a relatively stable rate, which was similar between the primary root and the lateral roots (Figure 3A). Thus, the cumulated number of lateral

roots that have emerged at a given distance of any root tip can be described by a linear relationship defined by a nude tip length and a slope determined by the average internode length.

Next, we investigated the length of lateral roots with respect to their position along the parental axis. The scattered data indicated a progressive but stochastic growth of laterals on the bearing axis (Figure 3B). Yet, first-order lateral roots showed a more pronounced growth than second-order lateral roots at a same distance of their respective parental root tip. We, therefore, established distinct length laws for the two orders of lateral roots.

These observations allowed us to deduce the parameters of a root model that can be used to generate RSAs. Using realistic ranges of nude tip length (between 5 and 35 mm) and average internode length (1–2.75 mm), we modeled the stochastic process of lateral root branching by a first-order Markov chain on growing root axes
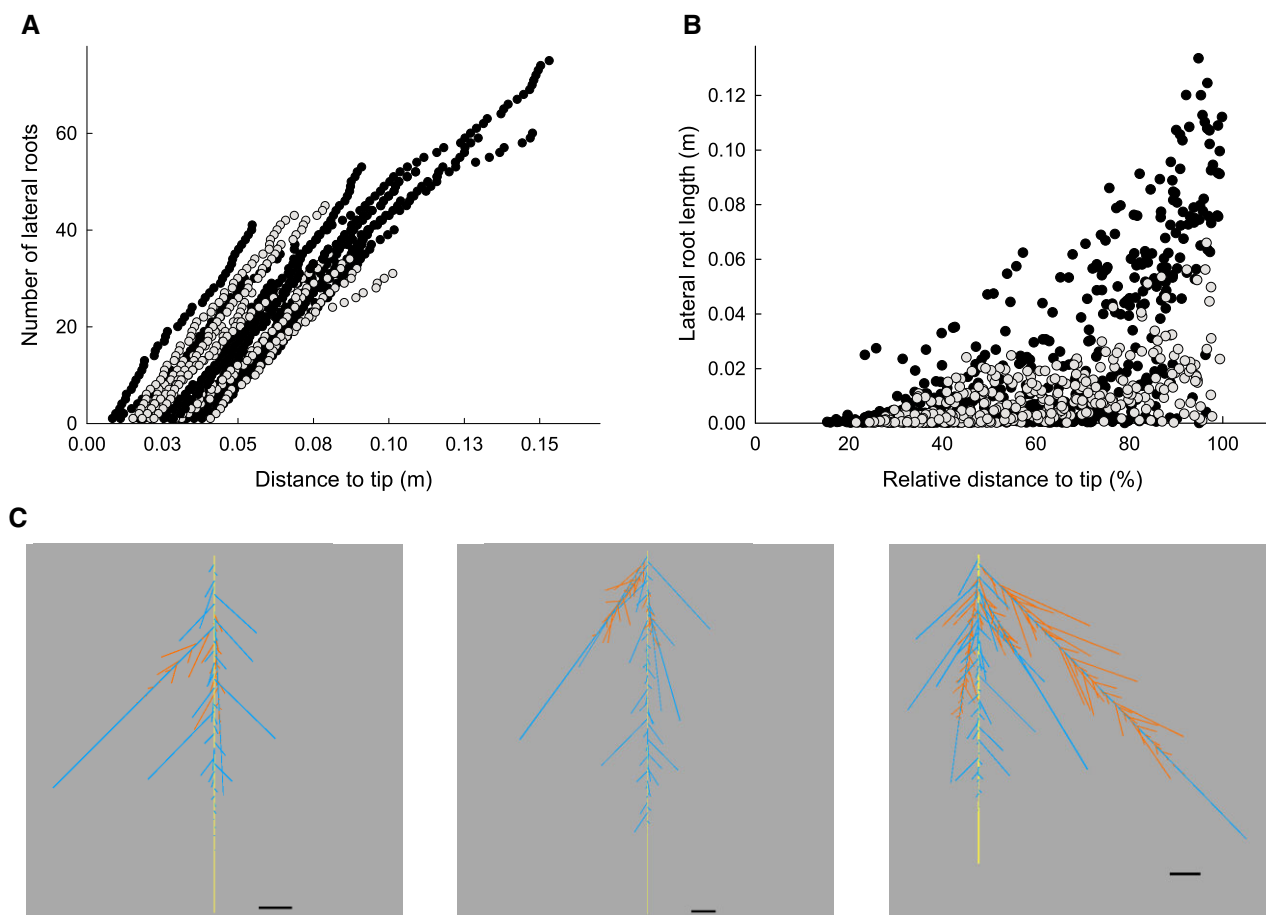
Figure 3 Organizing principles of Col-0 RSA. A, Profile of lateral formation along the parental root axis. The dots show the cumulated number of lateral roots formed at the indicated distance from the root tip, in individual primary (black) and first order lateral (gray) roots. B, Length of lateral root as a function of distance to tip of parental root. We observed that the absolute lengths of first order lateral roots (i.e. carried by the primary root) were very similar between plants of a same age, despite the variations in length shown by the primary root. Thus, plotting lateral root length as a function of the relative distance to the tip of the bearing axis provides a comprehensive description of lateral root length repartition. This representation was conserved in second order lateral roots, whose length was referred to the longest first-order lateral. (A) and (B) show cumulated data from 13 individual primary roots (black) and 9 first-order lateral roots (gray). C, Representative examples of simulated RSAs in (from left to right) the 25 percentile, median, and 75 percentile of total root length. Same color code for the primary root, the first order, and second order lateral roots as in Figure 1.

(Lucas et al., 2008). In addition, the length of simulated lateral roots was determined by fitting lateral root length along parental root axes (Figure 3B). Root diameters were set for each root order as indicated above. Setting the primary root length between 4 and 20 cm, we generated 9,520 RSAs that spanned the whole range of input parameters. Figure 3C illustrates the diversity of RSAs that can be generated using this pipeline.

Capturing features of RSAs using patterns of intercepted roots

In line with the cut-and-flow approach, we noted that phenotyping real RSAs by counting the number of roots that can be sectioned (intercepted) at six distances from their base (e.g. 80, 60, 45, 30, 20, 10 mm) was at least five times as fast as a full RSA reconstruction. The latter needs determining the nude tip length, position, and length of all lateral roots. By comparison, the number of intercepted roots at a few given distances from the base seems to be a more accessible yet informative indicator of RSA. Figure 4A illustrates intercept number curves derived from discrete cuts in real RSAs or from digitized Col-0 RSAs. These curves are overlapping with analogous intercept number curves, but derived from simulated RSAs.

Analysis of the full data set showed that cumulated intercepts were significantly correlated to architectural parameters of the root, such as the total root length (Supplemental Figure S5A). Another feature of these curves is that they cumulate intercept distributions of first and second-order lateral roots thereby capturing a key aspect of root branching (Figure 4B).

Finally, we wondered about the capacity of a determined intercept number profile to distinguish between markedly different RSAs. Supplemental Figure S5B shows a set of simulated RSAs that share intercept number profiles similar to those of reference real RSAs. The simulated RSAs were indeed very close, although with some variation, in their total root length (Figure 4C). The overall data establish that intercept number profiles allow to capture some fundamental features of RSAs.

Sensitivity analysis of root water transport to architecture and hydraulic parameters

Next, we applied the HydroRoot model to calculate the sap flow at a driving pressure of 0.3 MPa [$J_v(0.3 \, \text{MPa})$] in our collection of simulated RSAs using three distinct, yet realistic hydraulic configurations. For this, we selected three contrasting but uniform k values, all derived from cut-and-flow experiments, and applied a varying multiplying factor (ax) to the median axial conductivity (K) profile determined in the same approach (see Figure 2C). Thus, in addition to an intermediate hydraulic configuration (mean k value: 32.8 10^{-8} m s^{-1} MPa^{-1}; $ax = 1$), we defined a low hydraulic (minimal k: 9.9 10^{-8} m s^{-1} MPa^{-1}; $ax = 0.5$) and a high hydraulic (maximal k: 71.4 10^{-8} m s^{-1} MPa^{-1}; $ax = 2$) setting. The three sets of simulations derived from

these settings show a large range of $J_v(0.3 \, \text{MPa})$ values for RSAs of varying size (surface) and encompass the 20 experimentally determined $J_v(0.3 \, \text{MPa})$ values (Figure 5A).

The whole set of simulated RSA was used to explore the overall sensitivity of root water flow to elementary input architectural parameters. A dependency of $J_v(0.3 \, \text{MPa})$ on primary root length (Figure 5B) and average internode length (Figure 5C) can be observed whereas nude tip length (Figure 5D) had no impact on simulated flow. In the latter case, this means that the presence or absence of relatively short lateral roots close to the tip has a negligible impact on $J_v(0.3 \, \text{MPa})$. Finally, when the intermediate hydraulic setting was used, the variation range of all input architectural parameters was responsible for a variation of $J_v(0.3 \, \text{MPa})$ by about one order of magnitude.

$J_v(0.3 \, \text{MPa})$ was also dependent on variations in hydraulic parameters (Figure 6). Using the set of 9,520 simulated RSAs described above, we observed a positive and slightly saturating relationship between $J_v(0.3 \, \text{MPa})$ and k (Figure 6, A and B and Supplemental Figure S6A). A similar behavior was observed when varying ax values were applied to the whole axial conductivity (K) profile (Figure 6, A and C and Supplemental Figure S6B). These behaviors were not independent since sensitivity of $J_v(0.3 \, \text{MPa})$ to k or ax was higher and the saturation plateau was more pronounced when reference ax or k parameters were set to lower values (Figure 6A and Supplemental Figure S6). Thus, $J_v(P)$ seems to be co-limited by the radial and axial conductivity in a large range of values.

The strong dependence of K on vessel diameter, as indicated by Hagen–Poiseuille law, is usually interpreted to mean that the small vessels present at root tips are by far the most limiting (Steudle and Peterson, 1998). To examine this point in detail, we inspected the spatial variation of sap flow when a constant reducing factor ($ax < 1$) was applied throughout the K profile. Supplemental Figure S7 illustrates this approach on a representative RSA. Figure 6D summarizes the results, showing the relative variation of primary root axial flow at the indicated distance from root tip, under varying ax values. Although flow sensitivity was the highest close to root tip, we observed, for moderate axial limitations ($0.5 < ax < 1$), a pronounced and somewhat comparable impact of ax variation on axial flow all along the root. Thus, limitation of axial conductivity appears to be distributed over the whole primary root length. Since converging flows in a highly branched architecture may create marked hydraulic constraints in basal root sections, we also considered the simpler case of a cylindrical root harboring the same K profile as above (dashed lines, Figure 6D). Although axial flow was less sensitive to axial limitation ($ax < 1$) than in highly branched roots, a flow limitation along the whole root axis was also observed. These results emphasize the functional relevance of profiles with increasing K along the whole root axis, as determined by the cut-and-flow approach (Figure 2C).
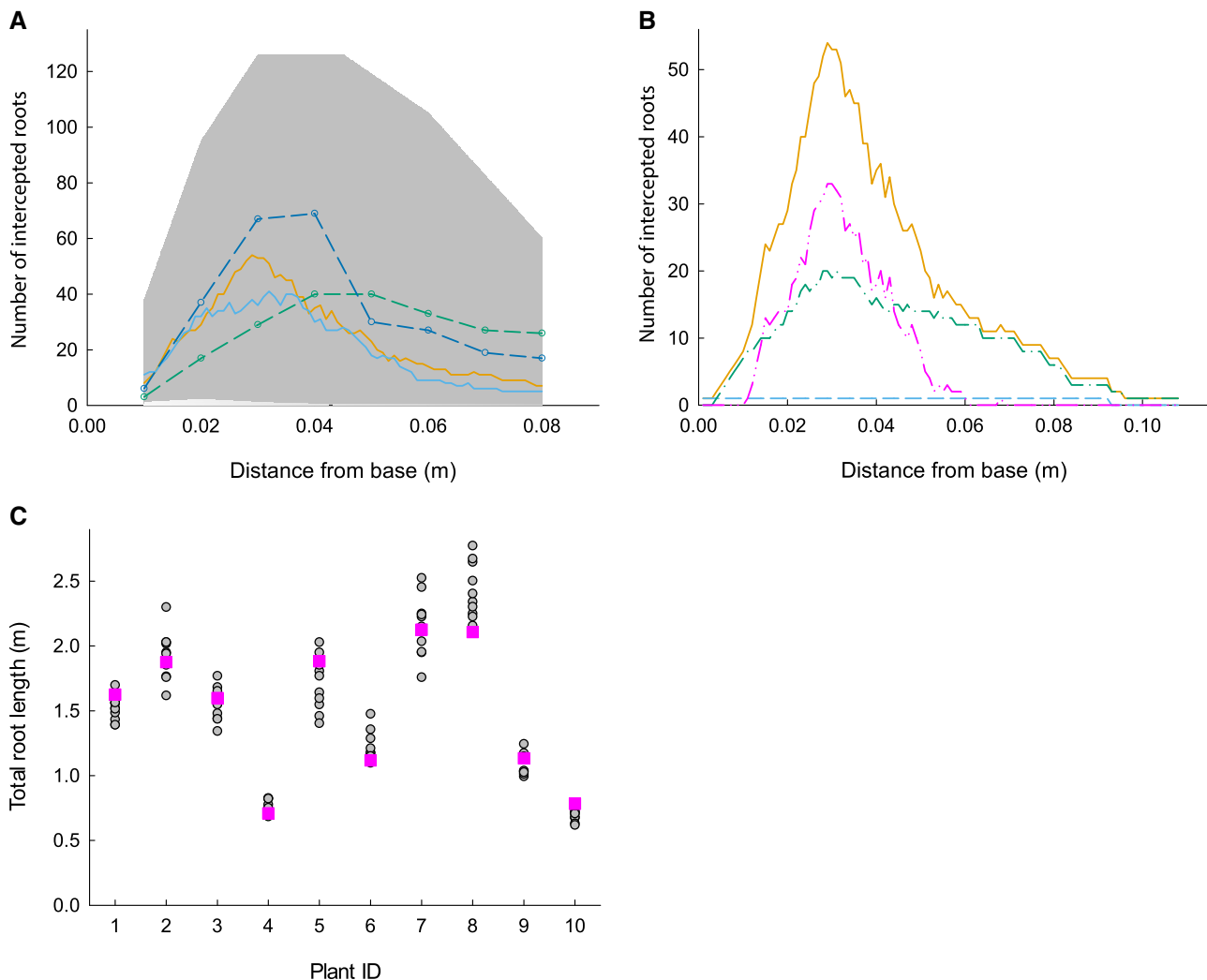
Figure 4 Intercept number profiles in real and simulated RSAs. A, Total number of intercepted roots at the indicated distance from the root base. Continuous lines correspond to experimental measurements of two real RSAs entirely digitized while dashed lines correspond to discrete measurements of two other real RSAs. The gray area delineates the whole set of intercept number curves derived from 9,520 simulated RSAs. Data are presented in a limited range of distances from tip (10–80 mm), to match the discrete experimental measurements. B, Profiles of first and second order intercepted lateral roots. Data from a RSA digitized from a real plant showing that the total intercept number curve (orange, continuous) can be decomposed into three curves representing the primary root (blue, dashed), and the first (green, dashed, one dot) and second (magenta, dashed two dots) order lateral roots. C, Relationship between total root length in 10 individual real plants (pink squares) and their close simulated RSAs (gray circles), screened by an absolute normalized difference in the intercepts at 10, 20, 30, 45, 60, and 80 mm from the tip. See example in Supplemental Figure S3B.

We then investigated possible interactions between hydraulic and architectural parameters in determining root water transport capacity (Supplemental Figure S8). For comparison of different hydraulic settings, corresponding J_v(0.3 MPa) flow values were centered using a normalizing factor. In such analyses, the relative response of J_v(0.3 MPa) to architectural input parameters was very similar between high ($k = 71.4 \ 10^{-8} \ \mathrm{m \ s^{-1} \ MPa^{-1}}$; $ax = 5$) and low ($k = 9.9 \ 10^{-8} \ \mathrm{m \ s^{-1} \ MPa^{-1}}$; $ax = 0.01$) hydraulic settings (Supplemental Figure S8).

Finally, we investigated the preferential sites of water uptake predicted in a whole root placed in a pressure chamber. Figure 6E represents a heatmap of simulated radial inflow (j_i, Figure 1C) throughout a typical RSA. Under intermediate

hydraulic conditions ($k = 32.8 \ 10^{-8} \ \mathrm{m \ s^{-1} \ MPa^{-1}}$; $ax = 1$), the highest radial flow is observed at the vicinity of the root base, in the primary root as well as the first-order lateral roots (Figure 6E, middle). A similar pattern is observed after increasing two-fold the axial conductance ($ax = 2$; Figure 6E, right). In contrast, water uptake by first-order lateral roots and downstream roots was strongly reduced under lower axial conductance ($ax = 0.125$; Figure 6E, left). When a non-uniform k profile was used (k was the highest in root tips and dropped three times to a lower plateau value in the differentiated zone; see above), radial inflow was enhanced in root tips but the remaining spatial pattern was comparable to that with uniform k (Supplemental Figure S4C). Overall, these analyses illustrate how the axial conductance can
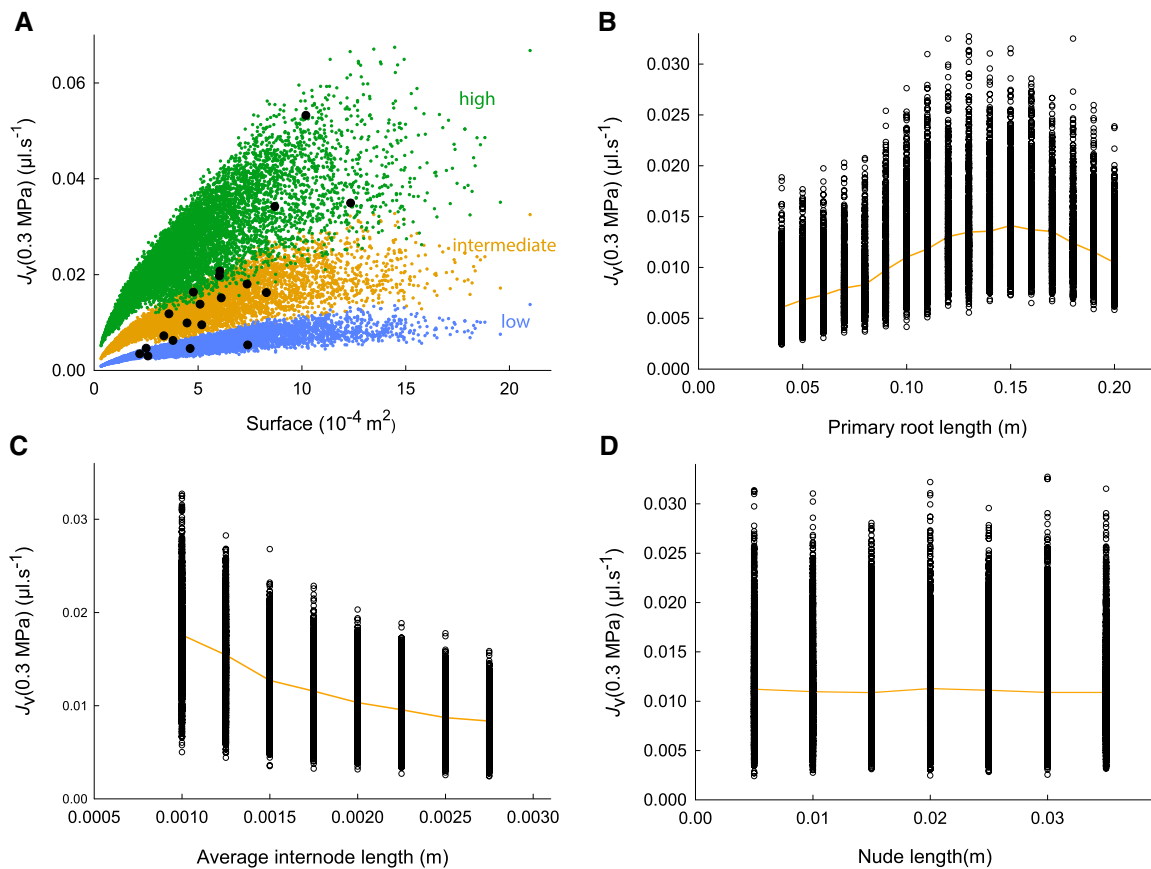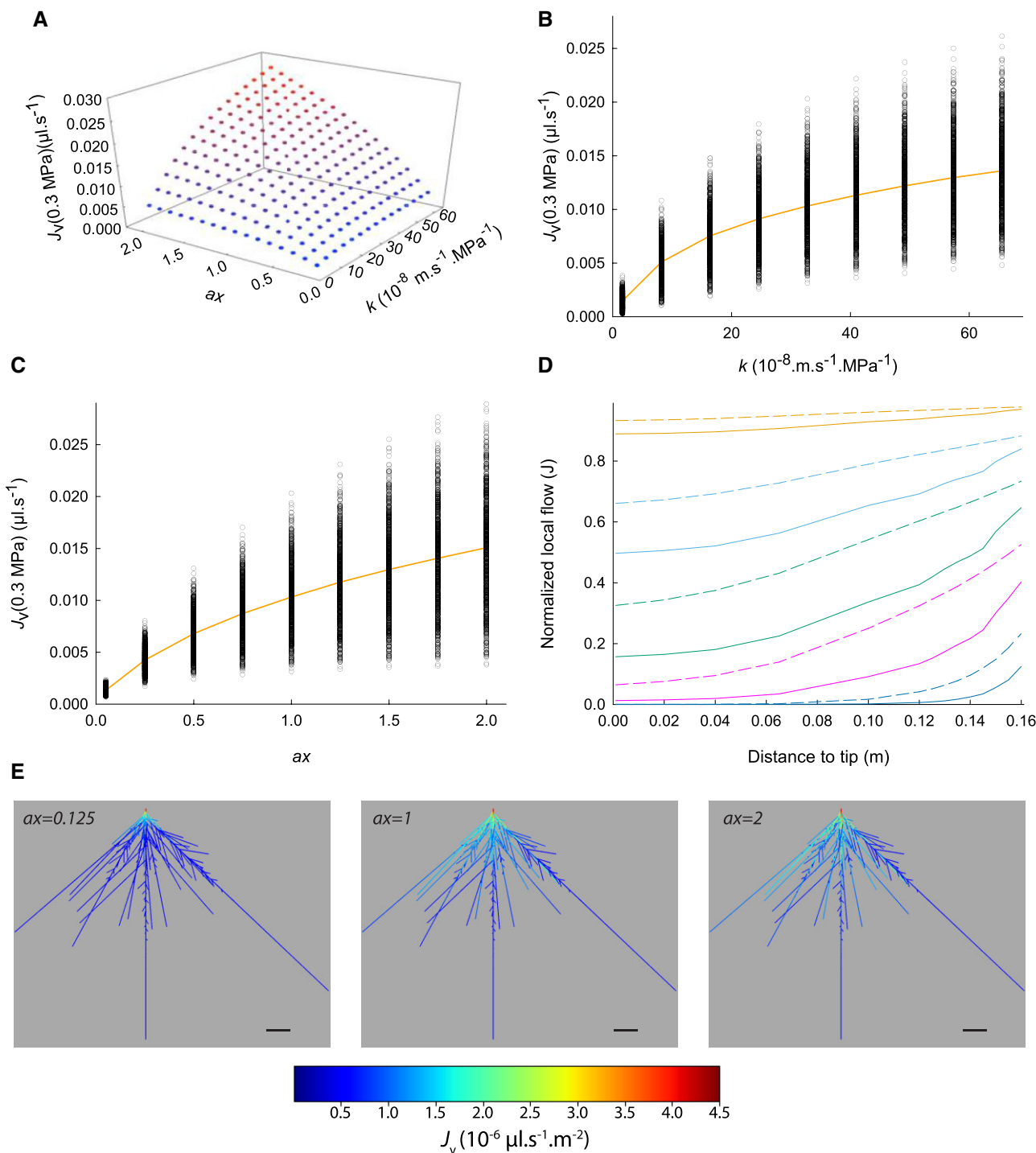
Figure 5 Sensitivity analysis of pressure-induced sap flow to RSA parameters. A, Root surface-to-flow relationship. The figure shows pressure-induced flow simulations ($J_V(0.3$ MPa)) for 9,520 RSAs harboring three distinct hydraulic configurations derived from cut-and-flow experiments (i) low (blue): minimal experimental k (9.86 10^{-8} m s^{-1} MPa^{-1}) and all values of median K profile reduced two-fold ($ax = 0.5$) (ii) intermediate (brown), mean k value (32.76 10^{-8} m s^{-1} MPa^{-1}) and median K profile (iii) high (green): maximal experimental k (71.43 10^{-8} m s^{-1} MPa^{-1}) and all values of median K profile enhanced two-fold ($ax = 2$). $J_V(0.3$ MPa) and root surface measured in 20 real RSAs (Table 1 and Figure 2D) are shown as black dots. B, Primary root length-to-flow relationship in 9,520 simulated RSAs harboring a mean k value (32.76 10^{-8} m s^{-1} MPa^{-1}) and median K profile. The median response curve is shown as a solid orange line. C, Dependency of $J_V(0.3$ MPa) on average internode length. Same procedures and conventions as in (B). D, Relationship between nude tip length and $J_V(0.3$ MPa). Same procedures and conventions as in (B).

influence the whole root hydraulic architecture and determine the relative contribution of the root basal and distal parts to whole root water uptake.

Dissecting the root hydraulic architecture of esk1 mutants

ESKIMO1 (ESK1) is a xylan-specific O-acetyltransferase (Yuan et al., 2013) which interferes with cellulose fibril organization and deposition of plant secondary cell walls. As a consequence, esk1 mutants exhibit an irregular xylem (irx) syndrome (Lefebvre et al., 2011). Here, we decided to re-examine the hydraulic defects observed in these mutants (Lefebvre et al., 2011) with a comprehensive analysis of their root hydraulic architecture, based on the numerical approach developed above. Morphological inspection of real plants of two allelic mutants of ESK1 (esk1-1, esk1-5) showed root growth alterations. While primary root growth was not different between genotypes, the intercept number profiles based on digitized RSAs of seven esk1-1 plants and seven esk1-5 plants highlighted, with respect to Col-0, a clear

reduction in root density in the 25–75 mm range from the base (Figure 7, A and B). This is attributable to a reduction in length of first-order laterals which translates into a deficit in second order laterals. Lefebvre et al. (2011) hypothesized from discrete anatomical cuts of the root that axial conductance might be reduced in esk1. We then used cut-and-flow experiments assisted by the HydroRoot model developed above to further characterize the hydraulic properties of esk1 roots. The analyses indicated that the median K of esk1-1 and esk1-5 was markedly reduced compared to Col-0 by factors from 1.6 up to 19.1 along the primary root axis (Figure 7C). The cut-and-flow approach also allowed us to estimate k, which, by comparison to Col-0, appeared to be reduced by 55%–33% in esk1-1 and esk1-5, respectively (Figure 7D) and by 40% ($P = 0.11$; Student's t test) in cumulated data from esk1-1 and esk1-5. Thus, in complement of an earlier report (Lefebvre et al., 2011), our results suggest that the loss of ESK1 function impacts not only xylem conductance, but also other determinants of root water transport capacity. More generally, this study shows how our

Figure 6 Sensitivity analysis of pressure-induced sap flow to hydraulic parameters. A, Dual dependency of J_v(0.3 MPa) on radial (k) and axial conductance (K). The latter is expressed as a multiplying factor (ax) applied to the median K profile. The figure shows J_v(0.3 MPa) variations in a representative RSA. B, Dependency of J_v(0.3 MPa) on k in a set of 9,520 RSAs, with fixed K ($ax = 1$). The median response curve is shown as a solid orange line. C, Dependency of J_v(0.3 MPa) on axial conductance (ax) in a same set of 9,520 RSAs, with fixed k (32.76 10^{-8} m.s^{-1}.MPa^{-1}). D, Effects of varying axial conductance profiles (ax) on primary root axial flow (J) at the indicated distance from root tip. The figure shows simulations for the same RSA as in (A) (solid lines) or an unbranched (cylindric) root (dotted lines). Orange: $ax = 0.95$; light blue: $ax = 0.75$; green: $ax = 0.5$; magenta: $ax = 0.25$; blue: $ax = 0.05$. All flow values are normalized with respect to the local flow observed in the same root and same position at $ax = 1$. E, Heat map representation of local radial flows for three levels of axial conductance (ax).
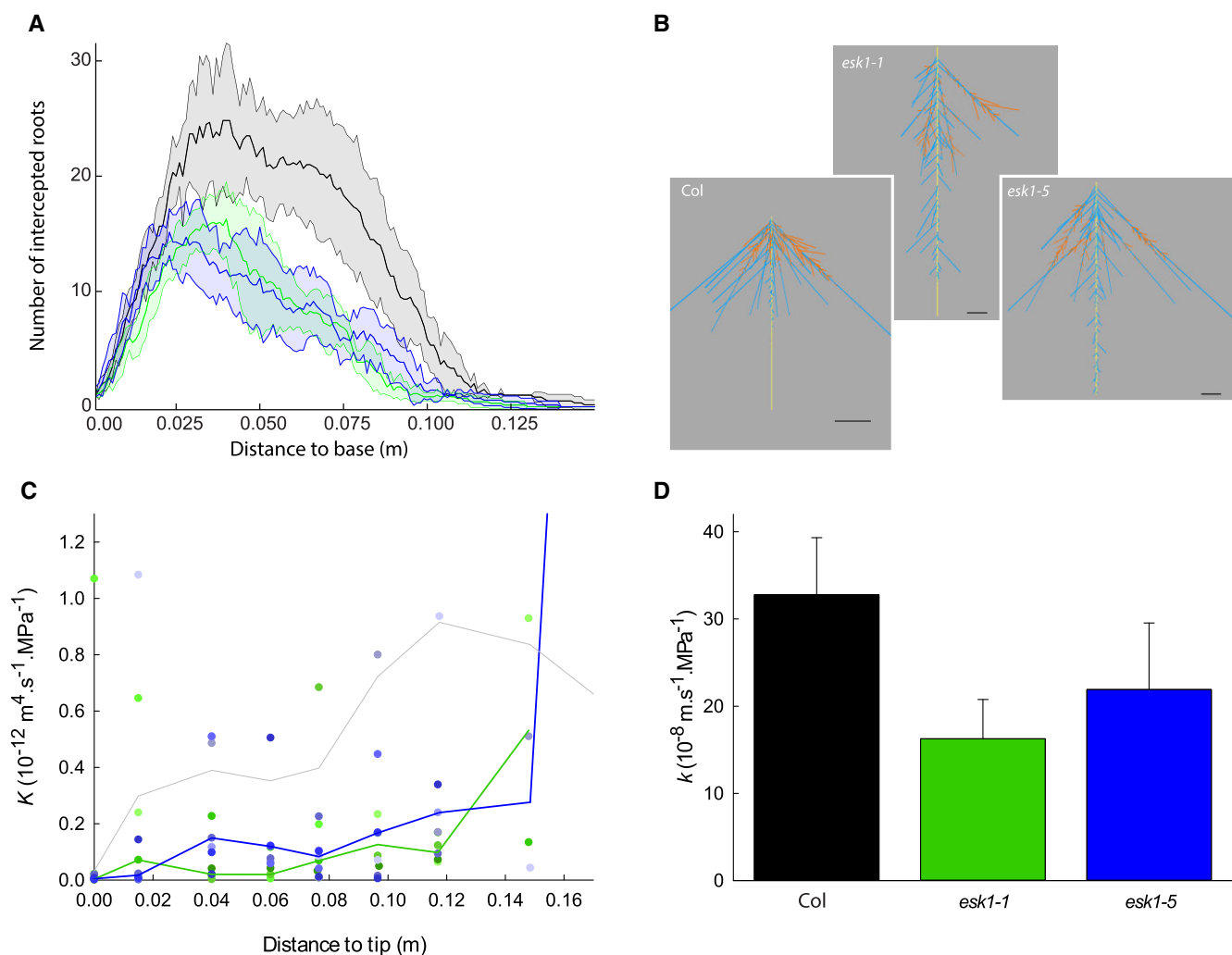
Figure 7 Root architecture and hydraulic phenotyping of *esk1* mutants. A, Total number of intercepted roots at the indicated distance from root base in Col-0 (black, $n = 6$), *esk1.1* (green, $n = 7$), and *esk1.5* (blue, $n = 7$). The figure shows, for each genotype, the mean curve and the envelope delineated by the 95% confidence interval for the number of intercepts at every mm. B, Representative RSAs of Col-0, *esk1.1* and *esk1.5* plants. The primary root, the first order and second order lateral roots are shown in blue, green, and red, respectively. C, Profile of axial conductance (K) along the root axis as determined from cut-and-flow experiments in *esk1.1* (green, $n = 5$) and *esk1.5* (blue, $n = 7$). The figure shows, for each genotype, measurements on individual plants and the corresponding median curve. The median curve of Col-0 (gray) is redrawn from Figure 2C. D, Corresponding radial conductivity values ($k \pm \mathrm{SE}$) (Col-0: $n = 10$; *esk1-1*: $n = 5$; *esk1.5*: $n = 7$).

model assisted phenotyping allows to dissect the Arabidopsis root hydraulic architecture into three major components (RSA, radial, and axial conductivities), and analyze their interplay in various genotypes.

Discussion

Investigating Arabidopsis root hydraulic architecture

Over the last two decades, the Arabidopsis root has emerged as a model of choice to address molecular and physiological aspects of aquaporin regulation (Boursiac et al., 2008; Lee et al., 2012), and more recently, to dissect plant tissue hydraulics by means of quantitative genetics (Shahzad et al., 2016; Tang et al., 2018). Although produced in adult plants, the data were interpreted using a simplified representation of the root as a single, continuous barrier between two homogeneous compartments: the soil solution and the xylem sap (Javot et al., 2003). Thus, the complexity and organizing principles of RSA in these plants, and their impacts on the root uptake capacity have not yet been addressed. By comparison, more elaborate root hydraulic models exist in other plant species such as maize and lupine (*Lupinus albus*) (Zarebanadkouki et al., 2016; Meunier et al., 2018), which are indeed more amenable than Arabidopsis to root water transport assays and anatomical dissection. With respect to these high-yielding crops, the wild species Arabidopsis exhibits moderate growth but comparable transpiration rates (Hosy et al., 2003; Yang et al., 2012; Macho-Rivero et al., 2017). Thus, it has been unclear whether its system of thin, highly branched roots is also hydraulically optimized for high water flows.

Here, we have investigated the organizing principles of Arabidopsis root hydraulic architecture, using interplay between experimental and computational modeling approaches. To ensure a maximal physiological meaning, experimental measurements and numerical simulations were performed at a water potential gradient (i.e. 0.3 MPa) consistent with water flows driven by transpiration under standard growth conditions. In addition, starting from a fine characterization of wild-type (Col-0) plants, our study was extended to possibly encompass a large panel of accessions and genotypes.

Our major concern was to understand the relative impact of elementary axial and radial hydraulic parameters on sap flow. Whereas confrontation of theoretical and experimental data through model sensitivity analysis remains the most common approach, there is a restricted number of studies whereby hydraulic parameters were deduced from inverse modeling and integration of architectural components (Doussan et al., 1998b, 2006; Zarebanadkouki et al., 2016; Meunier et al., 2018; Pascut et al., 2021;). While these earlier studies relied on functional analyses of individual axial roots of maize, lupine or Arabidopsis, we describe here a procedure based on cut-and-flow measurements for simultaneous determination of axial and radial conductance in highly branched root systems.

Assessing radial conductance

A direct experimental dissection of radial conductance components is, at present, not achievable. It would require an exact knowledge of the water potential across the root section and the experimental determination of elementary hydraulic conductivities corresponding to different transport pathways. Even though cell membrane permeability can be measured using cell pressure probe or protoplast swelling assays (Hüsken et al., 1978; Ramahaleo et al., 1999), all cell types are not amenable to these experimentations. Furthermore, the permeability of other components of radial water transport, such as the apoplast, has not been clearly determined yet (Buttersack and Basler, 1991). The present HydroRoot model proposes to synthetize the overall radial pathway through a single radial conductance (k) value. Here, we used an inverse modeling scheme similar to those developed in Arabidopsis and maize (Couvreur et al., 2018; Pascut et al., 2021) to determine k from RSA, $J_v(P)$, and K. In a simplified representation of Arabidopsis root anatomy, the outer tissues can be reduced to three concentric cylinders (cell layers) corresponding to the epidermis, cortex, and endodermis, with six cellular membranes in series. Cell pressure probe measurements in Col-0 cortical cells have given a cell membrane hydraulic conductivity of 1–$4 \ 10^{-6} \mathrm{m \ s^{-1} \ MPa^{-1}}$ (Boursiac et al., 2008; Sutka et al., 2011). We note that the order of magnitude of k determined in this work by inverse modeling ($3 \ 10^{-7} \mathrm{m \ s^{-1} \ MPa^{-1}}$) fits with one-sixth of this range, in agreement with the idea that radial water transport in the Arabidopsis root is predominantly mediated through cell membranes (aquaporins) (Tournaire-Roux et al., 2003).

Another line of simplification of HydroRoot is that, in most of our simulations, k was set constant from the root tip to base. Besides its simplicity, this hypothesis is supported by several studies, including a hydraulic dissection of developing maize roots through segment analysis (Frensch et al., 1996) and a hydraulic model inversion approach (Meunier et al., 2018) in young lateral and seminal roots of maize and lateral roots of lupine. Yet, plant roots show a progressive development of endodermal and peridermal barriers (Ranathunge and Schreiber, 2011; Doblas et al., 2017; Campilho et al., 2020; Calvo-Polanco et al., 2021) and longitudinal variations in aquaporin gene expression (Gambetta et al., 2013). Measurements of water uptake profiles in lupine or maize roots have also suggested a steady decrease of k over root length (Doussan et al., 1998b; Zarebanadkouki et al., 2016). Here, we investigated a two-step radial conductivity profile with a constant value of $3 \ k$ from tip to the appearance of full suberization and a value of k beyond. Our simulations indicate that this more realistic k representation does not impact the main conclusions on axial conductance (see below) drawn from HydroRoot running with uniform k values.

Assessing axial conductance

Most often, axial conductance is roughly evaluated using the Hagen–Poiseuille law and there are only a few instances where the axial conductance of roots was experimentally determined (Bramley et al., 2009; Frensch and Steudle, 1989; Meunier et al., 2018). The overall literature data indicate that the axial conductance can show a steep increase, from the root tip along the root axis, and most importantly varies between plant species, by up to five orders of magnitude (Meunier et al., 2018).

Here, we investigated the importance of axial conductance in the context of highly branched root systems. One first challenge was to develop a method for measuring K profiles throughout such complex root systems, where axial flow measurements in individual thin root axes are not feasible. However, microscopic observations suggested that K profile may be similar between root orders. This allowed us to reduce the problem to only one K profile. The cut-and-flow approach provided an efficient method, where the impact of multiple sections in roots of different orders was analyzed through a complex parameter optimization. We note that, because of its design, the cut-and-flow approach preferentially captures the features of axial transport and not radial transport. This is due to the fact that the progressive increase in sap flow observed upon successive cuts, which result in a progressive decrease in root surface, essentially reflects xylem vessel opening and suppression of resistance of corresponding root tips.

Surprisingly, the experimentally determined K profile indicated values that were up to 10 times lower than concomitant estimates using anatomical measurements together with Hagen–Poiseuille law. Frensch and Steudle (1989) and Sanderson et al. (1988) also found that the measured values were two to three times lower than the calculated ones, in

maize and barley (*Hordeum vulgare*) roots, respectively. Thus, it is likely that Hagen–Poiseuille estimates of single vessel conductance overlook the resistance due to connections between finite vessel elements, to possible vascular constrictions at the sites of root ramifications, or xylem surface properties (Sanderson et al., 1988; Shane et al., 2000). As elegantly modeled by Bouda et al. (2019), the failure of Hagen–Poiseuille estimates may also be due to the functioning of xylem as a network integrating resistive connections between functional vessels of distinct sizes.

Here, we further explored the importance of root axial conductance in a set of RSAs that were built, by extension, on well-defined parameters captured in real plants. Our analyses which extend the theoretical study of Bouda et al. (2018) show that highly branched root systems can show pronounced axial limitation for water transport. First, $J_V(P)$ showed a typical saturation in long root systems (with primary root length > 14 cm) (Figure 5B) which somewhat reflects the plateau shown by K along root length (Figure 2C). Increased root branching, while increasing the root surface to the same extent as root length, may not necessarily reveal an axial limitation in the first place (Figure 5C). However, spatially defined sensitivity analysis showed that hydraulic limitation due to xylem transport can occur along the whole root axis (Figure 6D). This may typically happen at the base of highly branched RSAs which convey converging flows from multiple root axes. Thus, although root tips truly represent particular sites for hydraulic limitation, our analyses show that the hydraulic load is somewhat spread over the whole root architecture. In other terms, the large metaxylem vessels present at root bases are not as oversized as initially claimed (Steudle and Peterson, 1998). A trade-off likely occurs on this trait as big vessels typically increase vulnerability of vascular tissues to cavitation (Tyree et al., 1994).

The conceptualization of water transport through sequential radial and axial water transport has somewhat led to independent estimates and functional analyses of the two processes. This approach may be misleading as this and a previous study show that water transport is actually co-limited by radial and axial conductances (Figure 6A; Zarebanadkouki et al., 2016). As a consequence, experimental determination of either one of these components strongly depends on the accuracy by which the other component is evaluated or truly measured. In physiological terms, our work indicates that real root systems can act on multiple cues to alter their water capacity. Interestingly, conductivity of the radial pathway can be adjusted over short or medium term through aquaporin regulation or root suberization whereas changes in RSA or vascular structures occur during much longer (days) adaptive responses of the root. Yet, these distinct traits have surely to be coordinately regulated, to ensure that root hydraulic architecture properly matches the plant's environmental conditions and developmental stages. Abscisic acid (ABA) was recently shown

to play such a coordinating role under water stress (Rosales et al., 2019).

Deciphering complex root phenotypes

Another major focus of our work was to work out the organizing principles of fully grown Arabidopsis root systems and dissect their branching properties. First, we showed that steady-state lateral root formation on a parent axis occurs over time and space in pretty well determined patterns that can be characterized using two constant parameters, nude tip length, and average internode length. Yet, the growth and arrest of lateral roots appeared as a highly stochastic process. Overall, this process was encapsulated in specific length laws thereby defining a complex pattern comprising several orders of lateral roots. In addition, our data set allowed to generate a set of virtual RSAs that covers real RSAs of distinct Arabidopsis genotypes. Conversely, it was critical for us to develop tools that would allow identifying the branching profiles of specific genotypes. Here, we show that intercept number profiles allow such kind of rapid and discriminative overview of RSA organization.

Earlier work has shown that defect in ESKIMO1 function results in xylem collapse. This phenotype was tentatively associated with a reduced Lp_r (Lefebvre et al., 2011). Since then, ESKIMO1 was shown to function as a xylan-specific O-acetyl transferase during secondary cell wall synthesis (Yuan et al., 2013; Grantham et al., 2017). Due to pleiotropic effects of cell wall alteration, *esk1* mutants also show enhanced ABA accumulation (Lefebvre et al., 2011) and constitutive defense responses (Escudero et al., 2017), which could both interfere with tissue hydraulics. Here, we chose *esk1* genotypes as typically complex cases and used our full set of hydraulic and architectural phenotyping and modeling approaches to revisit their root water uptake properties. In agreement with early anatomical work on xylem defects in this genotype, our study provides a quantitative estimate of reduction in axial conductance. Our analysis also pointed to a probable decrease in radial conductance (Figure 7D) and profound changes in root architecture (Figure 7, A and B). Thus, the reduced water uptake capacity of *esk1* results from more complex root alterations than initially thought. This example emphasizes the power of model-assisted hydraulic phenotyping which will prove extremely valuable in support of quantitative genetic analyses of root hydraulics (Shahzad et al., 2016; Tang et al., 2018). Along these lines, the MECHA model was recently used to infer distinct radial hydraulic profiles present in maize roots, either wild-type or with deregulated plasma membrane intrinsic protein 2;5 (Ding et al., 2020).

In conclusion, we have developed a model-assisted pipeline for accurate dissection of root hydraulic architectures in complex, highly branched root systems. While much emphasis has been put so far on aquaporin-mediated control of radial transport, our approach points to the complementary importance of axial hydraulic conductance. Drawbacks in inferring this conductance from anatomical measurements and the common idea that it is only limiting in root tips

have led to underestimating its importance. As a consequence, RSA is most often analyzed as the root foraging capacity for water whereas it can be associated with true hydraulic limitations. More generally, we have developed here a toolbox that can be used for dissecting the multiple root alterations that may interfere with root uptake capacity, in different genotypes (this work) and, by extension, in various environmental conditions. In particular, our study brings key tools to investigate, in Arabidopsis and possibly other species, the impact on root hydraulic architecture of environmental factors (e.g. drought) or hormones (e.g. ABA) acting on xylem differentiation (Ramachandran et al., 2020).

Materials and methods

Plant culture

Arabidopsis (*A. thaliana*) seeds were surface sterilized (7 min incubation in 86% [v/v] ethanol and 0.03% [v/v] chlorine followed by four washes with 70% [v/v] ethanol) and germinated onto a half-strength Murashige and Skoog medium with 0.9% (w/v) agar in square petri plates. Plates were incubated in a growth chamber with 70% humidity, 16-h light, 21°C for germination, and kept vertical for 10 days. Seedlings were then transferred to a hydroponic culture medium (1.25 mM KNO$_3$, 0.75 mM MgSO$_4$, 1.5 mM, Ca(NO$_3$)$_2$, 0.5 mM KH$_2$PO$_4$, 50 μM FeEDTA, 50 μM H$_3$BO$_3$, 12 μM MnSO$_4$, 0.70 μM CuSO$_4$, 1 μM ZnSO$_4$, 0.24 μM MoO$_4$Na$_2$, and 100 μM Na$_2$SiO$_3$) for 9–10 additional days in the same growth chamber. Col-0 (N70000), *eskimo1-1* (Xin and Browse, 1998), and *eskimo1-5* (SALK_089531) (Bouchabke-Coussa et al., 2008) plants were used in this study.

Digitalizing of root architectures

Excised root systems were spread out in a Petri dish containing a thin film of water and gently brushed prior to being digitized at 600–900 ppi with a desktop scanner. Images were analyzed with ImageJ software. For a given axis, internodes and lateral roots were traced back with straight or segmented lines, which were then saved in the ROI manager. This procedure was applied for the primary root as well as each lateral root carrying lateral roots, which resulted in a table containing the internodes and lateral roots length for each branched root.

Hagen–Poiseuille law estimate of axial conductance

The axial conductance along a root axis was estimated from direct observations of xylem vessels, using the Hagen–Poiseuille law applied to elliptic conduits. Root segments from the primary root, and first and second-order lateral roots were sampled every 2 cm, embedded in 7% (w/v) low-melting agarose and sliced with a vibratome. Slices were imaged under an optical microscope and xylem vessel dimensions were measured (Supplemental Figure S1A). Since vessel sections were not always circular but possibly oblong, vessel conductance (in m^4 s^{-1} MPa^{-1}) was computed according to the general formula for elliptic conduit conductance (Lewis and Boose, 1995):

$$K = \frac{(\pi \times a^3 \times b^3)}{64 \times \eta \times (a^2 + b^2)},$$

where *a* and *b* are long and short axis diameters (m), respectively, and η is the viscosity of water (1.10^{-3} Pa s at 20°C). In all cases, *a* was less than two times *b*.

Root water transport measurements

Root water transport was measured on de-topped plants with a set of pressure chambers, as in Javot et al. (2003). The hypocotyl of an excised root system was inserted into an adapter and sealed within the pressure chamber lid seal with silicone (Coltene Whaledent, France). The root was then placed into the pressure chamber in a container filled with filtered (20 μm) hydroponic solution. The adapter was connected to a flowmeter (Bronkhorst, France) in order to record the flow of sap from the hypocotyl. After a first pressurization of 10 min at 0.35 MPa, three successive flow measurements were taken at 0.32, 0.16, and 0.24 MPa. A linear fit of the flow-to-pressure relationship (with 0.92 < r^2 < 0.99) was used to deduce the sap flow at 0.3 MPa [J_v(0.3 MPa)].

Modeling principles

The HydroRoot model was developed in a Python programming language, as a component of the OpenAlea platform (Pradal et al., 2008, 2015). HydroRoot uses a MTG (Godin and Caraglio, 1998) to represent root hydraulic architecture, which consists of the topology of a root system (branching positions, root lengths, root radii, etc.) and its hydraulic structure (local radial and axial conductivities). The RSML format (Lobet et al., 2015) is used to import and export the data to/from the HydroRoot model. The model is open source and available through its public repository (https://github.com/openalea/hydroroot).

The hydraulic aspects of HydroRoot consisted in two main components: the radial water flow between the bathing solution and the xylem vessels and the axial transport through the xylem vessels. Following Doussan et al. (1998a, 1998b), the root was discretized as a network of elementary segments consisting of a microcircuit containing both radial (k_i) and axial (K_i) hydraulic conductances (Figure 1C). The local radial flux was written as $j_i = k_i(\psi_{e_i} - \psi_i)S_i$ and the local axial flow as $J_i = K_i(\psi_{out} - \psi_i)/L_i$, S_i and L_i being the surface area and the length of the elementary segments, respectively. By analogy with Ohm's law, both $1/(k_iS_i)$ and L_i/K_i may be modeled as electric resistances, and the hydraulic architecture may be assimilated to an electrical network (Doussan et al., 1998a; Prusinkiewicz et al., 2007). According to the boundary conditions (uniform pressure around the root and atmospheric pressure at its base), we are able to calculate the equivalent resistance of the network and then calculate the outflow rate. In brief, let us consider an elementary segment *i*, with $R_i = L_i/K_i$ and $r_i = 1/(k_iS_i)$ as axial and radial resistances, respectively. Its equivalent resistance R_{eq_i} is calculated as follows,

assuming that the apical equivalent resistance $R_{eq_{i-1}}$ is known:

$$\frac{1}{R_{eq_i}} = \frac{1}{R_{eq_{i-1}} + r_i} + \frac{1}{R_i}.$$

By implementing this equation, step by step from the tips, and by considering a branched root as a parallel network, we end up with an equivalent resistance for the whole network, and as a consequence, an equivalent hydraulic conductance K_{eq} (Prusinkiewicz et al., 2007; Albasha et al., 2019). The basal outgoing flux (J_v) is then calculated according to

$$J_v = K_{eq}(\psi_e - \psi_{base}).$$

Cut-and-flow experiments

An entire root system was excised and inserted into a pressure chamber, and water transport was measured as explained above, to check for the linearity of the flow-to-pressure relationship, but with a 10 µm filtered solution. If correct, the pressure was set to 0.3 MPa and the sap flow was recorded. After 3–5 min, the pressure was released and the root system was taken out of the pressure chamber and laid onto a 12×12 cm Petri dish filled with filtered hydroponic solution. All roots were stretched and aligned thereby allowing all longest root tip segments to be sectioned with a fresh razor blade, at 1–3 cm from the tip of the longest root. The remaining root system was put back in the pressure chamber at 0.3 MPa and flow measurement resumed for another 3–5 min. These steps (Supplemental Figure S2) were repeated three to eight times with the remaining tip segments of the root system being cut each time according to the same principle. Sap flow measured at 0.3 MPa for each cut step was then averaged and plotted against the cut position on the primary root (see Figure 2B as an example).

At each step, the released root segments and the remaining basal part of the root were digitized and processed to reconstruct the initial architecture of the measured root (Supplemental Figure S2). For each cut, roots segments were sorted in decreasing order of their total length (segment length plus the sum of its lateral root length, if any) and positioned accordingly on the primary root. Due to its diameter, the primary root was easily identified and could be attributed correctly for each cut. This allowed us to determine the position of each cut along the primary axis, and therefore reconstruct the whole RSA.

The final step of the whole procedure consisted in adjusting radial (k) and axial (K) conductances, to fit the sap flow measured after each cut. As mentioned above, K varies along each root axis with the distance to the tip. Here, K was represented as a linear piecewise function of nine points for an axis length up to 19.75 cm which corresponds to the longest root among those analyzed for anatomical data (Figure 2C). K was therefore represented by up to nine parameters. The radial conductivity k, which is set uniform

in our model, represented an additional parameter. Consequently, up to 10 parameters had to be adjusted from a data set of four to nine measurements. The system being underdetermined, we constrained the first derivative of K between two consecutive points to a minimum of -3.10^{-11} m^2 s^{-1} MPa^{-1}. This negative value represents the minimum observed on the lowess smoothing (Figure 2C). The fit was then performed by minimizing the sum of square of the residuals. The averaged radial conductivity from ten Col-0 plants (Table 1), k_{ini}, and the nine axial conductance data points from the lowess fit (Figure 2C), K_{ini}, were set as initial parameters. The most effective procedure was obtained following these steps:

- k_1 and K_1 were first estimated by adjusting two multiplying factors, ax and ar, with lower bounds of 10^{-20}, such that $k_1 = ar \times k_{ini}$ and $K_1 = ax \times K_{ini}$;
- keeping k_1, the axial conductance points were then adjusted (with the constraint above and with a nonnegative lower bound) from K_1, leading to K_2;
- keeping K_2, the radial conductivity was then adjusted from k_1 without bounds or constraint, leading to k_2;
- the k and K adjustment loop (steps 2 and 3) was repeated until the variation in radial conductivity falls below 10^{-10} m s^{-1} MPa^{-1}.

We used the function optimize.minimize of the SciPy Python library to perform these minimizations. The minimizations 1 and 2 were done with the default solver according to bounds and constraints whereas the minimization of the radial conductivity (step 3) was done with the "Nelder-Mead" solver. The robustness of the fitting procedure was eventually tested by starting from different initial parameters (Supplemental Figure S3).

Statistical analysis

All data sets were obtained in at least four independent biological repeats (plant cultures) with the indicated total number of plants. Pairwise comparisons of model parameters were performed using a Student t test ($P < 0.05$).

Accession numbers

Accession number of *ESK1* is At3g55990.

Supplemental data

The following materials are available in the online version of this article.

Supplemental Figure S1. Parameterization of root axial conductance using Hagen–Poiseuille law.

Supplemental Figure S2. Experimental details on the cut-and-flow procedure.

Supplemental Figure S3. Robustness of axial conductance curve estimation procedure.

Supplemental Figure S4. Influence of a two-step radial conductivity profile on simulated root water uptake.

Supplemental Figure S5. Relationship between cumulated number of intercepts and integrative properties of RSA.

Supplemental Figure S6. Dual dependency of $J_v(P)$ on radial (k) and axial conductance (K).

Supplemental Figure S7. Effects of varying axial conductance profiles (ax) on local axial flow (J).

Supplemental Figure S8. Sensitivity analysis of $J_v(0.3\,\text{MPa})$ to RSA parameters in two distinct hydraulic settings.

Supplemental Table S1. Parameters of HydroRoot model.

Funding

References

Albasha R, Fournier C, Pradal C, Chelle M, Prieto JA, Louarn G, Simonneau T, Lebon E (2019) HydroShoot: a functional-structural plant model for simulating hydraulic structure, gas and energy exchange dynamics of complex plant canopies under water deficit—application to grapevine (*Vitis vinifera*). In Silico Plants **1**: diz007

Barrowclough DE, Peterson CA, Steudle E (2000) Radial hydraulic conductivity along developing onion roots. J Exp Bot **51**: 547–557

Bouchabke-Coussa O, Quashie ML, Seoane-Redondo J, Fortabat MN, Gery C, Yu A, Linderme D, Trouverie J, Granier F, Téoulé E, et al. (2008) ESKIMO1 is a key gene involved in water economy as well as cold acclimation and salt tolerance. BMC Plant Biol **8**: 125

Bouda M, Brodersen C, Saiers J (2018) Whole root system water conductance responds to both axial and radial traits and network topology over natural range of trait variation. J Theor Biol **456**: 49–61

Bouda M, Windt CW, McElrone AJ, Brodersen CR (2019) In vivo pressure gradient heterogeneity increases flow contribution of small diameter vessels in grapevine. Nat Commun **10**: 5645

Boursiac Y, Boudet J, Postaire O, Luu DT, Tournaire-Roux C, Maurel C (2008) Stimulus-induced downregulation of root water transport involves reactive oxygen species-activated cell signalling and plasma membrane intrinsic protein internalization. Plant J **56**: 207–218

Boursiac Y, Chen S, Luu DT, Sorieul M, van den Dries N, Maurel C (2005) Early effects of salinity on water transport in *Arabidopsis* roots. Molecular and cellular features of aquaporin expression. Plant Physiol **139**: 790–805

Bramley H, Turner NC, Turner DW, Tyerman SD (2009) Roles of morphology, anatomy, and aquaporins in determining contrasting hydraulic behavior of roots. Plant Physiol **150**: 348–364

Buttersack C, Basler W (1991) Hydraulic conductivity of cell walls in sugar beet tissue. Plant Sci **76**: 229–237

Calvo-Polanco M, Ribeyre Z, Dauzat M, Reyt G, Hidalgo-Shrestha C, Diehl P, Frenger M, Simonneau T, Muller B, Salt DE, et al. (2021) Physiological roles of Casparian strips and suberin in the transport of water and solutes. New Phytol **232**: 2295–2307

Campilho A, Nieminen K, Ragni L (2020) The development of the periderm: the final frontier between a plant and its environment. Curr Opin Plant Biol **53**: 10–14

Couvreur V, Faget M, Lobet G, Javaux M, Chaumont F, Draye X (2018) Going with the flow: multiscale insights into the composite nature of water transport in roots. Plant Physiol **178**: 1689–1703

Danjon F, Reubens B (2008) Assessing and analyzing 3D architecture of woody root systems, a review of methods and applications in tree and soil stability, resource acquisition and allocation. Plant Soil **303**: 1–34

Di Pietro M, Vialaret J, Li G, Hem S, Rossignol M, Maurel C, Santoni V (2013) Coordinated post-translational responses of aquaporins to abiotic and nutritional stimuli in *Arabidopsis* roots. Mol Cell Proteomics **12**: 3886–3897

Ding L, Milhiet T, Couvreur V, Nelissen H, Meziane A, Parent B, Aesaert S, Van Lijsebettens M, Inze D, Tardieu F, et al. (2020) Modification of the expression of the aquaporin *Zm*PIP2;5 affects water relations and plant growth. Plant Physiol **182**: 2154–2165

Doblas VG, Geldner N, Barberon M (2017) The endodermis, a tightly controlled barrier for nutrients. Curr Opin Plant Biol **39**: 136–143

Doussan C, Pages L, Vercambre G (1998a) Modelling of the hydraulic architecture of root systems: an integrated approach to water absorption—model description. Ann Bot **81**: 213–223

Doussan C, Pierret A, Garrigues E, Pages L (2006) Water uptake by plant roots: II—modelling of water transfer in the soil root-system with explicit account of flow within the root system—comparison with experiments. Plant Soil **283**: 99–117

Doussan C, Vercambre G, Pages L (1998b) Modelling of the hydraulic architecture of root systems: an integrated approach to water absorption—distribution of axial and radial conductances in maize. Ann Bot **81**: 225–232

Draye X, Kim Y, Lobet G, Javaux M (2010) Model-assisted integration of physiological and environmental constraints affecting the dynamic and spatial patterns of root water uptake from soils. J Exp Bot **8**: 2145–2155

Escudero V, Jorda L, Sopena-Torres S, Melida H, Miedes E, Munoz-Barrios A, Swami S, Alexander D, McKee LS, Sanchez-Vallet A, et al. (2017) Alteration of cell wall xylan acetylation triggers defense responses that counterbalance the immune deficiencies of plants impaired in the beta-subunit of the heterotrimeric G-protein. Plant J **92**: 386–399

Foster KJ, Miklavcic SJ (2016) Modeling root zone effects on preferred pathways for the passive transport of ions and water in plant roots. Front Plant Sci **7**: 914

Frensch J, Hsiao TC, Steudle E (1996) Water and solute transport along developing maize roots. Planta **198**: 348–355

Frensch J, Steudle E (1989) Axial and radial hydraulic resistance to roots of maize (*Zea mays* L.). Plant Physiol **91**: 719–726

Gambetta GA, Fei J, Rost TL, Knipfer T, Matthews MA, Shackel KA, Walker MA, McElrone AJ (2013) Water uptake along the length of grapevine fine roots: developmental anatomy, tissue-specific aquaporin expression, and pathways of water transport. Plant Physiol **163**: 1254–1265

Godin C, Caraglio Y (1998) A multiscale model of plant topological structures. J Theor Biol **191**: 1–46

Godin C, Costes E, Sinoquet H (1999) A method for describing plant architecture which integrates topology and geometry. Ann Bot **84**: 343–357

Grantham NJ, Wurman-Rodrich J, Terrett OM, Lyczakowski JJ, Stott K, Iuga D, Simmons TJ, Durand-Tardif M, Brown SP, Dupree R, et al. (2017) An even pattern of xylan substitution is critical for interaction with cellulose in plant cell walls. Nat Plants **3**: 859–865

Heymans A, Couvreur V, Lobet G (2021) Combining cross-section images and modeling tools to create high-resolution root system hydraulic atlases in *Zea mays*. Plant Direct **5**: e334

Hosy E, Vavasseur A, Mouline K, Dreyer I, Gaymard F, Poree F, Boucherez J, Lebaudy A, Bouchez D, Very AA, et al. (2003) The

Arabidopsis outward K+ channel GORK is involved in regulation of stomatal movements and plant transpiration. Proc Natl Acad Sci USA 100: 5549–5554

Hüsken D, Steudle E, Zimmermann U (1978) Pressure Probe Technique for Measuring Water Relations of Cells in Higher Plants. Plant Physiol 61: 158–163

Javaux M, Couvreur V, Vanderborght J, Vereecken H (2013) Root water uptake: from three-dimensional biophysical processes to macroscopic modeling approaches. Vadose Zone J 12: 1–16

Javot H, Lauvergeat V, Santoni V, Martin-Laurent F, Guclu J, Vinh J, Heyes J, Franck KI, Schäffner AR, Bouchez D, et al. (2003) Role of a single aquaporin isoform in root water uptake. Plant Cell 15: 509–522

Jones H, Leigh RA, Jones RGW, Tomos AD (1988) The integration of whole-root and cellular hydraulic conductivities in cereal roots. Planta 174: 1–7

Klein SP, Schneider HM, Perkins AC, Brown KM, Lynch JP (2020) Multiple integrated root phenotypes are associated with improved drought tolerance. Plant Physiol 183: 1011–1025

Knipfer T, Fricke W (2011) Water uptake by seminal and adventitious roots in relation to whole-plant water flow in barley (Hordeum vulgare L.). J Exp Bot 62: 717–733

Lee SH, Chung GC, Jang JY, Ahn SJ, Zwiazek JJ (2012) Overexpression of PIP2;5 aquaporin alleviates effects of low root temperature on cell hydraulic conductivity and growth in Arabidopsis. Plant Physiol 159: 479–488

Lefebvre V, Fortabat MN, Ducamp A, North HM, Maia-Grondard A, Trouverie J, Boursiac Y, Mouille G, Durand-Tardif M (2011) ESKIMO1 disruption in Arabidopsis alters vascular tissue and impairs water transport. PLoS ONE 6: e16645

Lewis AM, Boose ER (1995) Estimating volume flow rates through xylem conduits. Am J Bot 82: 1112–1116

Lobet G, Pound MP, Diener J, Pradal C, Draye X, Godin C, Javaux M, Leitner D, Meunier F, Nacry P, et al. (2015) Root system markup language: toward a unified root architecture description language. Plant Physiol 167: 617–627

Lucas M, Guedon Y, Jay-Allemand C, Godin C, Laplaze L (2008) An auxin transport-based model of root branching in Arabidopsis thaliana. PLoS ONE 3: e3673

Lynch JP (2013) Steep, cheap and deep: an ideotype to optimize water and N acquisition by maize root systems. Ann Bot 112: 347–357

Macho-Rivero MA, Camacho-Cristobal JJ, Herrera-Rodriguez MB, Muller M, Munne-Bosch S, Gonzalez-Fontes A (2017) Abscisic acid and transpiration rate are involved in the response to boron toxicity in Arabidopsis plants. Physiol Plant 160: 21–32

Maurel C, Nacry P (2020) Root architecture and hydraulics converge for acclimation to changing water availability. Nat Plants 6: 744–749

Meunier F, Couvreur V, Draye X, Vanderborght J, Javaux M (2017a) Towards quantitative root hydraulic phenotyping: novel mathematical functions to calculate plant-scale hydraulic parameters from root system functional and structural traits. J Math Biol 75: 1133–1170

Meunier F, Couvreur V, Draye X, Zarebanadkouki M, Vanderborght J, Javaux M (2017b) Water movement through plant roots—exact solutions of the water flow equation in roots with linear or exponential piecewise hydraulic properties. Hydrol Earth Syst Sci 21: 6519–6540

Meunier F, Draye X, Vanderborght J, Javaux M, Couvreur V (2017c) A hybrid analytical-numerical method for solving water flow equations in root hydraulic architectures. Appl Math Model 52: 648–663

Meunier F, Zarebanadkouki M, Ahmed MA, Carminati A, Couvreur V, Javaux M (2018) Hydraulic conductivity of soil-grown lupine and maize unbranched roots and maize root-shoot junctions. J Plant Physiol 227: 31–44

Pascut FC, Couvreur V, Dietrich D, Leftley N, Reyt G, Boursiac Y, Calvo-Polanco M, Casimiro I, Maurel C, Salt DE, et al. (2021) Non-invasive hydrodynamic imaging in plant roots at cellular resolution. Nat Commun 12: 4682

Postaire O, Tournaire-Roux C, Grondin A, Boursiac Y, Morillon R, Schäffner T, Maurel C (2010) A PIP1 aquaporin contributes to hydrostatic pressure-induced water transport in both the root and rosette of Arabidopsis. Plant Physiol 152: 1418–1430

Pradal C, Dufour-Kowalski S, Boudon F, Fournier C, Godin C (2008) OpenAlea: a visual programming and component-based software platform for plant modelling. Funct Plant Biol 35: 751–760

Pradal C, Fournier C, Valduriez P, Cohen-Boulakia S (2015) OpenAlea: scientific workflows combining data analysis and simulation. In G Amarnath, R Susan, eds, Proceedings of the 27th International Conference on Scientific and Statistical Database Management (San Diego, USA). ACM, New York, Article 11, pp 1–6

Prusinkiewicz P, Allen M, Escobar-Gutierrez A, DeJong TM (2007) Numerical methods for transport-resistance sink-source allocation models. Frontis 22: 123–137

Ramachandran P, Augstein F, Nguyen V, Carlsbecker A (2020) Coping with water limitation: hormones that modify plant root xylem development. Front Plant Sci 11: 570

Ramahaleo T, Morillon R, Alexandre J, Lassalles J-P (1999) Osmotic Water Permeability of Isolated Protoplasts. Modifications during Development. Plant Physiol 119: 885–896

Ranathunge K, Schreiber L (2011) Water and solute permeabilities of Arabidopsis roots in relation to the amount and composition of aliphatic suberin. J Exp Bot 62: 1961–1974

Rosales MA, Maurel C, Nacry P (2019) Abscisic acid coordinates dose-dependent developmental and hydraulic responses of roots to water deficit. Plant Physiol 180: 2198–2211

Sanderson J, Whitbread FC, Clarkson DT (1988) Persistent xylem cross-walls reduce the axial hydraulic conductivity in the apical 20 cm of barley seminal root axes—implications for the driving force for water-movement. Plant Cell Environ 11: 247–256

Shahzad Z, Canut M, Tournaire-Roux C, Martinière A, Boursiac Y, Loudet O, Maurel C (2016) A potassium-dependent oxygen sensing pathway regulates plant root hydraulics. Cell 167: 87–98

Shane MW, McCully ME, Canny MJ (2000) Architecture of branch-root junctions in maize: structure of the connecting xylem and the porosity of pit membranes. Ann Bot 85: 613–624

Steudle E (2001) The cohesion-tension mechanism and the acquisition of water by plant roots. Annu Rev Plant Physiol Plant Mol Biol 52: 847–875

Steudle E, Jeschke WD (1983) Water transport in barley roots—measurements of root pressure and hydraulic conductivity of roots in parallel with turgor and hydraulic conductivity of root cells Planta 158: 237–248

Steudle E, Peterson CA (1998) How does water get through roots? J Exp Bot 49: 775–788

Sutka M, Li G, Boudet J, Boursiac Y, Doumas P, Maurel C (2011) Natural variation of root hydraulics in Arabidopsis grown in normal and salt stress conditions. Plant Physiol 155: 1264–1276

Tang N, Shahzad Z, Lonjon F, Loudet O, Vailleau F, Maurel C (2018) Natural variation at XND1 impacts root hydraulics and trade-off for stress responses in Arabidopsis. Nat Commun 9: 3884

Tixier A, Cochard H, Badel E, Dusotoit-Coucaud A, Jansen S, Herbette S (2013) Arabidopsis thaliana as a model species for xylem hydraulics: does size matter? J Exp Bot 64: 2295–2305

Tournaire-Roux C, Sutka M, Javot H, Gout E, Gerbeau P, Luu DT, Bligny R, Maurel C (2003) Cytosolic pH regulates root water transport during anoxic stress through gating of aquaporins. Nature 425: 393–397

Tyree MT, Davis SD, Cochard C (1994) Biophysical perspectives of xylem evolution: is there a tradeoff of hydraulic efficiency for vulnerability to dysfunction? IAWA J 15: 335–360

Xin Z, Browse J (1998) *Eskimo1* mutants of Arabidopsis are constitutively freezing-tolerant. Proc Natl Acad Sci USA **95**: 7799–7804

Yang Z, Sinclair TR, Zhu M, Messina CD, Cooper M, Hammer GL (2012) Temperature effect on transpiration response of maize plants to vapour pressure deficit. Environ Exp Bot **78**: 157–162

Yuan Y, Teng Q, Zhong R, Ye ZH (2013) The Arabidopsis DUF231 domain-containing protein ESK1 mediates 2-O- and 3-O-acetylation of xylosyl residues in xylan. Plant Cell Physiol **54**: 1186–1199

Zarebanadkouki M, Kroener E, Kaestner A, Carminati A (2014) Visualization of root water uptake: quantification of deuterated water transport in roots using neutron radiography and numerical modeling. Plant Physiol **166**: 487–499

Zarebanadkouki M, Meunier F, Couvreur V, Cesar J, Javaux M, Carminati A (2016) Estimation of the hydraulic conductivities of lupine roots by inverse modelling of high-resolution measurements of root water uptake. Ann Bot **118**: 853–864

Zwieniecki MA, Thompson MV, Holbrook NM (2003) Understanding the hydraulics of porous pipes: tradeoffs between water uptake and root length utilization. J Plant Growth Regul **21**: 315–323